Cascade-Targeting Poly(amino acid) Nanoparticles Eliminate Intracellular Bacteria via On-Site Antibiotic Delivery

Wenli Feng, Guofeng Li,* Xiaoxu Kang, Ruibai Wang, Fang Liu, Dongdong Zhao, Haofei Li, Fanqiang Bu, Yingjie Yu, T. Fintan Moriarty, Qun Ren, and Xing Wang*

Intracellular bacteria in latent or dormant states tolerate high-dose antibiotics. Fighting against these opportunistic bacteria has been a long-standing challenge. Herein, the design of a cascade-targeting drug delivery system (DDS) that can sequentially target macrophages and intracellular bacteria, exhibiting on-site drug delivery, is reported. The DDS is fabricated by encapsulating rifampicin (Rif) into mannose-decorated poly(α-N-acryloyl-phenylalanine)-*block*-poly(β-N-acryloyl-D-aminoalanine) nanoparticles, denoted as Rif@FAM NPs. The mannose units on Rif@FAM NPs guide the initial macrophage-specific uptake and intracellular accumulation. After the uptake, the detachment of mannose in acidic phagolysosome via Schiff base cleavage exposes the D-aminoalanine moieties, which subsequently steer the NPs to escape from lysosomes and target intracellular bacteria through peptidoglycan-specific binding, as evidenced by the in situ/ex situ co-localization using confocal, flow cytometry, and transmission electron microscopy. Through the on-site Rif delivery, Rif@FAM NPs show superior in vitro and in vivo elimination efficiency than the control groups of free Rif or the DDSs lacking the macrophages- or bacteria-targeting moieties. Furthermore, Rif@FAM NPs remodel the innate immune response of the infected macrophages by upregulating M1/M2 polarization, resulting in a reinforced antibacterial capacity. Therefore, this biocompatible DDS enabling macrophages and bacteria targeting in a cascade manner provides a new outlook for the therapy of intracellular pathogen infection.

1. Introduction

Intracellular bacteria are able to multiplicate inside host cells and manipulate their biology, resulting in a number of globally serious infections including tuberculosis, endocarditis, osteomyelitis, necrotizing pneumonia, and sepsis.[1] Treatment often requires long-term and intensive antibiotics administration; however, treatment failure and relapse are unfortunately common.[2] As we currently understand it, the major reasons for the failure of clinical therapy to eradicate intracellular bacteria include: i) poor cellular membrane penetration, suboptimal intracellular accumulation, and short retention of antibiotics;[3] ii) diminished antibacterial activity of antibiotics because of the harsh acidic and hydrolytic environment within phagolysosomes;[4] iii) intracellular bacteria being in a dormant state and tolerance of otherwise lethal concentration of antibiotics;[5] and iv) bacteria escape from phagolysosomes and hide in privileged intracellular compartments that evade the bactericidal actions of antibiotics.[6] At later timepoints, potentially after the cessation of therapy, the bacteria may then proliferate resulting in the apoptosis and autophagy of the cells. The evasive bacteria re-enter the circulation or re-infect local tissues.[7] As such, the infected cells have been likened to "Trojan horses" that protect bacteria with later dissemination of the infection into deeper tissues.[8]

Drug delivery systems (DDSs) have shown increasing potential for the treatment of intracellular bacterial infection.[9] The

W. Feng, G. Li, X. Kang, D. Zhao, H. Li, F. Bu, Y. Yu, X. Wang
State Key Laboratory of Organic-Inorganic Composites
Beijing Laboratory of Biomedical Materials
Beijing University of Chemical Technology
Beijing 100029, P. R. China
E-mail: ligf@mail.buct.edu.cn; wangxing@mail.buct.edu.cn
R. Wang
State Key Laboratory for Infectious Disease Prevention and Control
National Institute for Communicable Disease Control and Prevention
Chinese Center for Disease Control and Prevention
Beijing 102206, P. R. China

F. Liu
Department of Oncology of Integrative Chinese and Western Medicine
China-Japan Friendship Hospital
Beijing 100029, P. R. China
T. F. Moriarty
AO Research Institute Davos
Davos 7270, Switzerland
Q. Ren
Empa
the Swiss Federal Laboratories for Materials Science and Technology
Laboratory for Biointerfaces
Lerchenfeldstrasse 5, St. Gallen 9014, Switzerland

**ADVANCED
SCIENCE NEWS**
www.advancedsciencenews.com

**ADVANCED
MATERIALS**
www.advmat.de

most common approach is increasing specificity of the DDS to facilitate cellular antibiotics accumulation.[10] They are functionalized by cellular targeted ligands, such as mannose and galactose, for the effective intracellular delivery of antibiotics.[9c,11] In order to improve the stability of the antibiotics within the cells, the controlled release of antibiotics in responding to natural stimuli (e.g., pH, enzyme, redox) has been described.[12] However, these approaches may not work when the intracellular bacteria are in a dormant state or hiding in the vacuole, in which the intracellular bacteria are able to withstand high-dose antibiotics.[13] To fight against these stubborn bacteria, delivering antibiotics to the bacterial residing locations is considered to be a more feasible approach. To date, the study of on-site antibiotic delivery via intracellular bacteria targeting is still in its infancy.[14] Thus, such an approach, targeting both the host cells and intracellular bacteria in a cascade, could offer optimal efficacy against intracellular bacterial infection.[15]

Recently, we synthesized a series of poly(N-acryloyl amino acid)s using a robust photoinduced electron/energy transfer-reversible addition-fragmentation chain transfer (PET-RAFT) polymerization technique.[16] The poly(N-acryloyl amino acid)s are considered promising DDSs because of their excellent biocompatibility and tunable morphologies and functionalities.[17] Moreover, the poly(N-acryloyl amino acid)s display an appealing drug loading efficiency as their abundant non-covalent

interactions with drugs.[17a] With this inspiration, here we propose a new protocol to cascade-target intracellular methicillin-resistant *Staphylococcus aureus* (MRSA) and on-site deliver antibiotics based on poly(N-acryloyl amino acid) (**Scheme 1**). Different from previous studies, β-N-acryloyl-D-aminoalanine was first used as the key monomer to synthesize poly(α-N-acryloyl-phenylalanine)-*block*-poly(β-N-acryloyl-D-aminoalanine) (denoted as FA), which was in favor of introducing high-density D-aminoalanine pendants. Subsequently, mannose was conjugated with α-amino of the D-aminoalanine pendants via Schiff base to prepare mannose-decorated poly(α-N-acryloyl-phenylalanine)-*block*-poly(β-N-acryloyl-D-aminoalanine) (denoted as FAM). Rifampicin (Rif), a hydrophobic antibiotic, was then loaded into assembled FAM nanoparticles (NPs) and a novel cascade-targeting DDS (namely Rif@FAM NPs) fabricated. The Rif@FAM NPs preferentially entered macrophages by a mannose receptor-mediated endocytosis process, increasing intracellular accumulation of Rif. The subsequent pH-triggered detachment of the mannose in the acidic phagolysosomes led to the formation of Rif@FA NPs. Sequentially, the exposed D-aminoalanine moieties then enabled the resulting Rif@FA NPs to escape into the cytoplasm and anchor the MRSA by peptidoglycan-specific binding. On-site Rif@FA NPs released the Rif precisely regardless of the states and locations of the intracellular MRSA, overcoming antibiotics
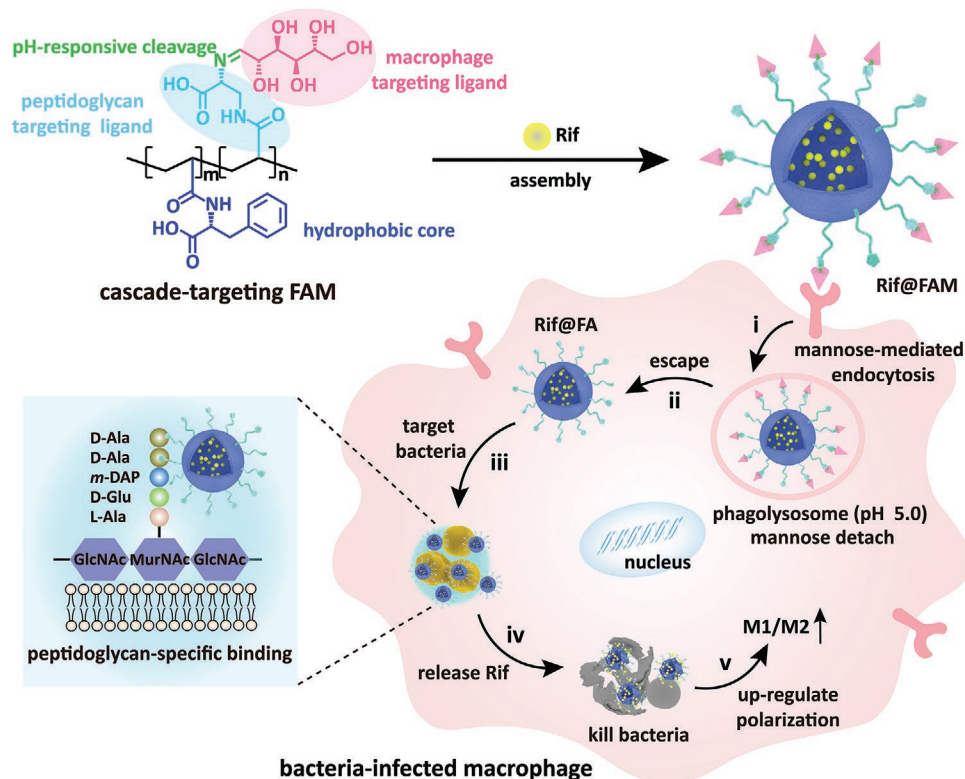
Scheme 1. The cascade-targeting DDS eliminates intracellular MRSA. Cascade-targeting FAM consists of 3 parts: 1) Poly(α-N-acryloyl-phenylalanine) (PF) as the hydrophobic core; 2) poly(β-N-acryloyl-D-aminoalanine acid) (PA) as the bacteria targeting ligand; and 3) mannose as the macrophage targeting ligand. The cascade-targeting process of the DDS is divided into 5 steps: i) Rif@FAM NPs selectively enter macrophages by mannose-mediated endocytosis; ii) mannose is detached in acidic phagolysosomes via the dynamic Schiff base. The exposed D-aminoalanine moieties steer the resulting Rif@FA NPs to escape into the cytoplasm; iii) Rif@FA NPs anchor the intracellular bacteria by peptidoglycan-specific binding; iv) Rif@FA NPs release the Rif to kill intracellular bacteria; and v) upregulation of M1/M2 polarization.

tolerance. Furthermore, Rif@FAM NPs modulated the innate immune responses of macrophages by upregulating the M1/M2 polarization to reinforce the antibacterial effect. Therefore, this cascade-targeting DDS, enabling on-site antibiotic delivery and precise antibacterial treatment, could greatly improve the therapeutic efficiency of stubborn intracellular bacterial infections.

2. Results and Discussion

2.1. Synthesis and Characterization of Polymers and DDS

The synthesis and assembly of the cascade-targeting DDS are shown in **Figure 1**A. The amphiphilic FAM copolymer was synthesized by two-step reactions. First, poly(N-acryloyl amino acid), that is, poly(α-N-acryloyl-phenylalanine)-*block*-poly(β-N-acryloyl-α-*Boc*-D-aminoalanine) (denoted as FA_{Boc}), was synthesized using PET-RAFT polymerization technique (Scheme S1, Supporting Information).[17a] α-N-acryloyl-phenylalanine and β-N-acryloyl-α-*Boc*-D-aminoalanine were used as the monomers and synthesized in an amidation reaction, confirming by ^{1}H/^{13}C NMR and electrospray ionization mass spectra (Figure S1, Supporting Information). PF was synthesized by PET-RAFT polymerization using 2-(dodecylthiocarbonothioylthio)-2-methylpropionic acid (DDMAT) as RAFT agent, tris[2-phenyl-pyridinato-C²,N]iridium(III) (Ir(ppy)₃) as photoinitiator and α-N-acryloyl-phenylalanine as monomers. Subsequently, the obtained PF was applied as the micro-RAFT agent to the synthesis of FA_{Boc} copolymer. According to the ^{1}H NMR and GPC, the molecular weights of PF and FA_{Boc} were calculated to be ≈7100 ($M_w/M_n = 1.3$) and ≈11 000 g mol^{-1} ($M_w/M_n = 1.4$, Figures S2 and S3, and Table S1, Supporting Information), respectively; for FA_{Boc}, the ratio of polymerization degree between PF and poly(β-N-acryloyl-α-*Boc*-D-aminoalanine) segments was 28:14 (Figure S2, Supporting Information). During the second step, the protection group *Boc* was removed to
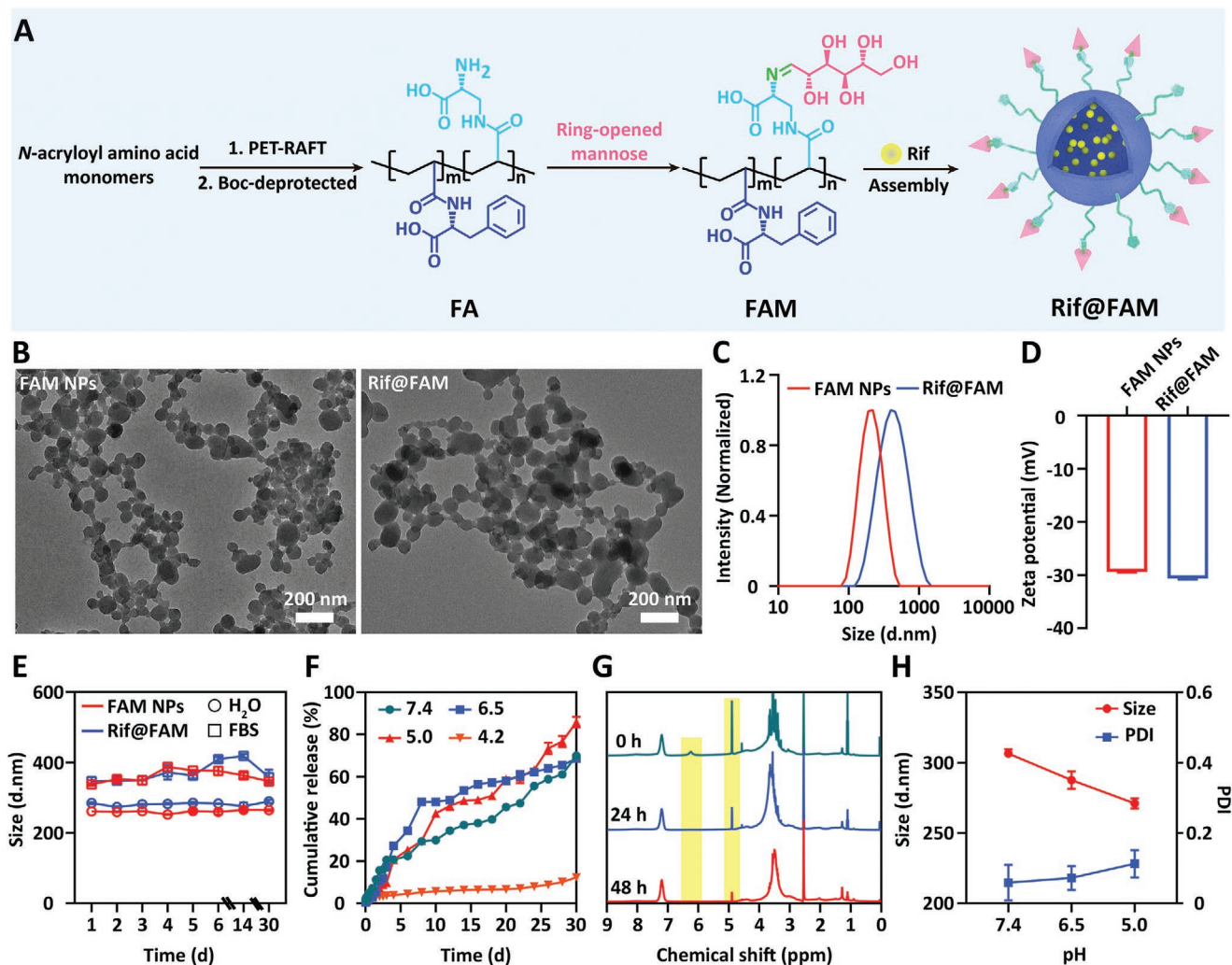
Figure 1. Characterization of copolymers and DDS. A) Schematic illustration of the formation of Rif@FAM NPs. B) TEM images, C) DLS, and D) zeta potential of FAM and Rif@FAM NPs in PBS. E) Stability assay of FAM and Rif@FAM NPs in diverse media, $n = 3$. F) Release profiles of the Rif from Rif@FAM NPs at various pHs, $n = 3$. G) ^{1}H NMR spectra of FAM polymer before and after acidic treatment (pH 5.0) for 24 and 48 h. The shaded peaks indicated the integrals of characteristic hydroxyl protons of the ring-opened mannose grafting on FAM. H) Sizes and PDI of Rif@FAM NPs against various pHs, $n = 3$.

release free α-amino groups in FA, which was further functionalized by ring-opened mannose via Schiff base. ^{1}H NMR analysis confirmed there were 8 mannose molecules binding with FA, namely FAM (Figure S2, Supporting Information). FTIR and XPS spectra further verified the successful grafting of mannose (Figure S4, Supporting Information). Meanwhile, the single-targeting control polymers for either macrophages-targeted purpose (i.e., poly(α-N-acryloyl-phenylalanine)-block-poly(2-(α-D-mannosyloxy) ethyl acrylate), denoted as FM) or bacteria-targeted purpose (FA) were synthesized and characterized using the similar method (Figures S2 and S5, Supporting Information).

Rif@FAM NPs were prepared via self-assembly of FAM in a solvent system of DMSO/water (1/9, v/v) containing Rif (Figure 1A). Blank FAM NPs were prepared as control and exhibited uniform spherical morphology (Figure 1B) with an average diameter of 250 nm as revealed by DLS (Figure 1C). After loading Rif, the obtained Rif@FAM NPs maintained their spherical morphology (Figure 1B) with a slightly increased diameter of 280 nm (Figure 1C). Their zeta potentials varied from −29.4 to −30.6 mV after loading Rif (Figure 1D). Meanwhile, the corresponding FA and FM NPs were prepared and characterized according to the same methods and exhibited similar characteristics (Figure S6, Supporting Information). The results of the stability test showed that there was no significant change in both the size and the polymer dispersity index (PDI) of Rif@FAM NPs over 30 days (Figure 1E and Figure S7, Supporting Information), suggesting the good stability of the DDS. The drug loading content of Rif@FAM NPs reached up to ≈18.9 wt% (Table S2, Supporting Information). Drug release profiles of Rif@FAM NPs were further investigated (Figure 1F). Solvents with different pHs were selected to mimic the phagolysosomes environment.[18] It revealed that the Rif was continuously released from Rif@FAM NPs for more than 1 month with the pH between 5.0 and 7.4. Compared with Rif@FAM NPs, free Rif exhibited a rapid drug release property. Approximately 87.7% of Rif was released from the free Rif group in 12 h (Figure S8, Supporting Information). This implied that Rif@FAM NPs would be in favor of eliminating intracellular bacteria by a long-term continuous antibiotics release. Besides, release efficiency increased in a lower pH environment, attributed to the detachment of mannose from FAM through Schiff base dissociation.[19] In order to confirm this hypothesis, ^{1}H NMR was used to investigate the chemical structure of the FAM before and after the treatment of the acidic solution at pH 5.0. The results showed that the peaks of the mannose group sharply decreased, demonstrating the stimuli-responsive characteristic of FAM (Figure 1G). Additionally, Rif@FAM NPs exhibited decreased sizes and increased zeta potentials at pH 6.4 and 5.0 compared with pH 7.4, also confirming the detachment of mannose (Figure 1H and Figure S9, Supporting Information). Nevertheless, Rif@FAM NPs could maintain a stable size distribution after the detachment of the mannose groups in the harsh acidic environment. One interesting phenomenon was that a dramatic decline of the drug release rate was exhibited at pH 4.2 (Figure 1F), most likely attributed to the aggregation of FAM NPs.[20] A turbidity study further revealed that FAM NPs were soluble under neutral conditions as well as in highly acidic conditions (pH < 2.2); but at pH 2.2–4.5, they were insoluble

(Figure S10, Supporting Information). This was consistent with the result of the increased size of Rif@FAM NPs at pH 4.2 (Figure S11, Supporting Information).

2.2. Mannose-Mediated Endocytosis In Vitro

First, the cytotoxicity of Rif@FAM NPs toward Tohoku Hospital Pediatrics-1 (THP-1) macrophages and human embryonic kidney cell line 293 (HEK293) cells was tested. Rif@FAM NPs showed low cytotoxicity at wide-range Rif dosages of ≤40 μg mL^{-1} (Figure S12, Supporting Information), indicating their cytocompatibility. Subsequently, Nile Red (NR), as a model dye, was encapsulated into the NPs (i.e., NR@FAM and NR@FA NPs) to monitor the time-dependent cellular uptake by confocal laser scanning microscope (CLSM). THP-1 macrophages were labeled by NR@FAM NPs after 0.5 h incubation and prolonged incubation to 2 h led to a significant increase of the mean fluorescence intensity (MFI, **Figure 2**A,B), which was ≈2.3 times higher than that of the control group, NR@FA NPs (without mannose modification, ****, $p = 0.000003$, Figure 2B). Further extending incubation time (4, 8, 12 h), the cellular uptake of NR@FAM NPs showed a time-dependent enhancement, while that of NR@FA NPs reached saturation at 8 h (Figure 2C and Figure S13, Supporting Information), suggesting the specific internalization of NR@FAM NPs. To validate the mannose-mediated endocytosis pathway of NR@FAM NPs in macrophages, a competitive inhibition experiment was conducted.[21] Free mannose was used as an endocytosis inhibitor and co-incubated with THP-1 for 1 h before treatment with NR@FAM NPs. Free mannose significantly inhibited the cellular uptake of NR@FAM NPs, showing a dose-dependent inhibitory effect (Figure 2D and Figure S14, Supporting Information), whereas it had no effect on the internalization of NR@FA NPs (Figure S14, Supporting Information). These results demonstrated that the mannose inhibitor competitively prevented the entry of NR@FAM NPs by occupying mannose receptors on the surfaces of THP-1 macrophages.

To examine the selective targeting ability of NR@FAM NPs toward macrophages,[22] we further investigated their cellular uptake in THP-1 and HEK293 cells co-culture system. THP-1 macrophages were stained with green fluorescence by calcein acetoxymethyl ester (calcein AM) prior to co-culture with HEK293 cells. The NR@FAM NPs were then added to the THP-1 and HEK293 co-culture plate. After a 0.5 h incubation, the red signals of NR@FAM NPs coexisted with the calcein AM green positive THP-1 macrophages, whilst only weak red fluorescence signals were observed in HEK293 cells (Figure 2E). After 1 h incubation, most of the NR@FAM NPs were found in the THP-1 macrophages, showing strong fluorescence intensity, while an extremely low fluorescence intensity was detected in HEK293 cells (white arrows in Figure 2E). Fluorescence co-localization between NR@FAM NPs and THP-1 macrophages was analyzed by software *image J*. The red signals of NR@FAM NPs overlayed well with the green signals of the THP-1 macrophages. (PCC and OCV were higher than ≈60%, and reached up to ≈80% at a 1 h co-incubation (Figure 2F,G). These results strongly suggested that the proposed FAM DDS has an excellent macrophage-targeting activity.

ADVANCED
SCIENCE NEWS
www.advancedsciencenews.com

ADVANCED
MATERIALS
www.advmat.de

Figure 2. Mannose-mediated endocytosis. A) Confocal images of THP-1 macrophages incubated with NR, NR@FA, and NR@FAM NPs at 10 μg mL^{-1} with different times; diamidine phenyl indole (DAPI) was used to labled the cell nucleus. B) The corresponding MFI of cellular uptake calculated using Image J software, $n > 6$. C) MFI of NR in THP-1 macrophages determined by flow cytometry after incubation with NR@FA and NR@FAM NPs at 10 μg mL^{-1} with different times, $n = 3$. D) MFI of internalized NR@FAM NPs with 1 h pre-treatment with different doses of competitive inhibitor mannose, $n = 3$. E) Confocal images of HEK293 cells and THP-1 macrophages after co-incubation with NR@FAM NPs (10 μg mL^{-1}) with different times. THP-1 macrophages were labeled in green, and NPs were labeled in red. The white arrows denoted the HEK293 cells. F) Co-localization analyses on the fluorescence between THP-1 macrophages and NR@FAM NPs, evaluated by Pearson's correlation coefficient (PCC) and overlap coefficient value (OCV), $n = 3$. G) Co-localization fluorescence intensity profiles between NR@FAM NPs and THP-1 macrophages after 1 h co-incubation, analyzed using Image J software. * $p < 0.05$, ** $p < 0.01$, *** $p < 0.001$, **** $p < 0.0001$, and ns $p > 0.05$, respectively.

**ADVANCED
SCIENCE NEWS**

www.advancedsciencenews.com

**ADVANCED
MATERIALS**

www.advmat.de

2.3. Bacterial Targeting and Extracellular Antibacterial Activity

D-alanine is the basic unit of bacterial peptidoglycan. D-alanine and its analogs (e.g., D-aminoalanine) are well-established peptidoglycan-targeting molecules for antibacterial chemotherapy.[23] Thus, bacterial targeting of the designed NPs with the presence of D-aminoalanine moieties was investigated. In terms of this, FA NPs were selected to perform this investigation since they were formed through the detachment of the mannose after the cellular uptake (**Figure 3**). It was observed by the SEM images that many more FA NPs anchored on the surface of MRSA after co-incubation when compared to the control group without FA NPs treatment (Figure 3A). It was also demonstrated by the TEM images, showing a rough membrane edge of the MRSA with FA NPs treatment (Figure 3B). Subsequently, co-localization of FA NPs and MRSA was analyzed by CLSM to further validate bacterial targeting.[24] The NR@FA NPs exhibited red fluorescence signals (Figure 3C), and overlapped well with MRSA in green fluorescence signals stained by fluorescein isothiocyanate (FITC, Figure 3D and Figure S15, Supporting Information), suggesting a good targeting effect of FA NPs in contrast to FM NPs (Figure S16, Supporting Information). Previous studies have revealed that macromolecules or peptides containing a D-alanine terminal can insert into the bacterial cell wall and interface the biosynthesis of peptidoglycan of bacteria.[25] To demonstrate the effect of bacterial dormant states on the targeting property of FA NPs, a temperature-regulated phagocytosis experiment was carried out (Figure 3E and Figure S17, Supporting Information). FITC dye loaded FA NPs (denoted as FITC@FA NPs) were co-incubated with MRSA at 37 °C. The fluorescence intensity of MRSA significantly enhanced with the increase of co-incubation time, but, as the incubation temperature decreased to 4 °C, the fluorescence intensity was significantly decreased (*, $p = 0.04$ at 0.5 h and *, $p = 0.02$ at 3 h). This was mainly due to the growth arrest of MRSA at low temperature; whereby the metabolism of peptidoglycan and the phagocytosis of the FITC@FA NPs would be slowed down.[26] Nevertheless, the interaction between FITC@FA NPs and bacteria could be continuously enhanced regardless of the bacterial growth period. Furthermore, FA NPs would competitively inhibit the growth of MRSA. In the presence of FA NPs, the bacterial proliferation was suppressed in the logarithmic growth phase. Growth inhibition increased with increasing concentration of FA NPs (Figure 3F), suggesting that FA NPs could competitively inhibit bacterial peptidoglycan synthesis by blocking the receptor of D-alanine.

Subsequently, Rif@FA and Rif@FAM NPs were used to investigate their MIC. The results indicated that the MIC values of Rif@FA, Rif@FAM NPs, and the free Rif were 7 ng mL^{-1} (Figure S18, Supporting Information), but the CFUs treated by Rif@FA NPs were significantly lower than that of free Rif under 2 × MIC and 5 × MIC (**, $p = 0.004$ for 2 × MIC and ****, $p = 0.00006$ for 5 × MIC, Figure 3G,H), implicating the good killing effect of Rif@FA NPs against MRSA. Rif@FAM NPs showed similar antibacterial performance with Rif@FA NPs (ns, $p = 0.62$ and 0.05 for 2 × and 5 × MIC, respectively) because of mannose detachment from FAM NPs under the bacterial acidic microenvironment.[27] SEM analysis (Figure S19, Supporting Information) further confirmed that Rif@FA and Rif@FAM NPs could anchor the cell wall of MRSA and exhibited an antibacterial effect by disrupting or deforming the membranes of MRSA.

2.4. Intracellular Bacteria Targeting and Antibacterial Activity

Intracellular MRSA targeting of FAM NPs was characterized using in-situ/ex-situ co-localization assays. First, the NR@NPs were incubated for 24 h with THP-1 macrophages pre-infected with FITC-labeled MRSA, and the nuclei of the THP-1 cells were stained with blue fluorescence by DAPI after co-incubation. As shown in **Figure 4**A, MRSA successfully infected THP-1 cells and dispersed in the cytoplasm. The distributions of NR@FAM NPs depended on the locations of MRSA. The red fluorescence signals of NR@FAM NPs matched well with the green fluorescent of MRSA, exhibiting a bright yellow fluorescence when merged. 3D CLSM showed that NR@FAM NPs bound with MRSA in stereo space vision (Figure 4B), further confirming intracellular MRSA targeting of NR@FAM NPs.[28] In contrast, NR@FM NPs evenly distributed around the nuclei of THP-1 cells, regardless of the locations of intracellular MRSA. 3D renderings clearly showed that the fluorescence signals between NR@FM NPs and MRSA did not overlap (Figure 4B). NR@FM NPs could target THP-1 macrophages by mannose-receptor, but they could not specifically track the invading MRSA because there was no specific binding effect with the absence of D-aminoalanine moieties. Subsequently, MRSA-infected THP-1 macrophages were lysed by 0.1% Triton X-100, and the intracellular MRSA were extracted and detected by CLSM (Figure 4C). Interestingly, CLSM images showed a perfect fluorescence overlap between NR@FAM NPs and the MRSA despite the intensive processes of lysis and extraction. This implied that high-density D-aminoalanine enhanced the binding ability between NR@FAM NPs and MRSA, excluding the possibility of off-targeting effects. Conversely, NR@FM NPs were in separate compartments with the MRSA, and MRSA-FM co-localization was rarely observed (Figure 4C). Quantitative analysis by flow cytometry assay revealed that the MFI of the intracellular MRSA in the group of NR@FAM NPs was ≈3 times higher than that of NR@FM NPs (Figure 4D). Corresponding TEM images further confirmed that plenty of NR@FAM NPs bound to the surface of the intracellular MRSA, suggesting the specific intracellular-bacteria targeting of NR@FAM NPs (Figure 4E). In situ TEM imaging for the MRSA-infected THP-1 macrophages showed that MRSA in phagolysosomes of macrophages maintained a complete and clean cell wall (Figure 4F). After FAM NPs treatment, they were observed to bind on the surface of the invading MRSA (blue arrows in Figure 4G). But for FM NPs treatment, no NPs could be found around the intracellular MRSA (Figure 4H). To further determine the drug delivery capacity of FAM NPs, MRSA-infected THP-1 macrophage treated with Rif@FAM NPs was observed by in situ TEM (Figure S20, Supporting Information). After Rif@FAM NPs treatment, the infected macrophage exhibited a complete cellular morphology with abundant bacterial fragments in its phagolysosomes. Differently, the infected macrophage treated with Rif@FM NPs was in a collapsed state accompanied by the survival MRSA. Such
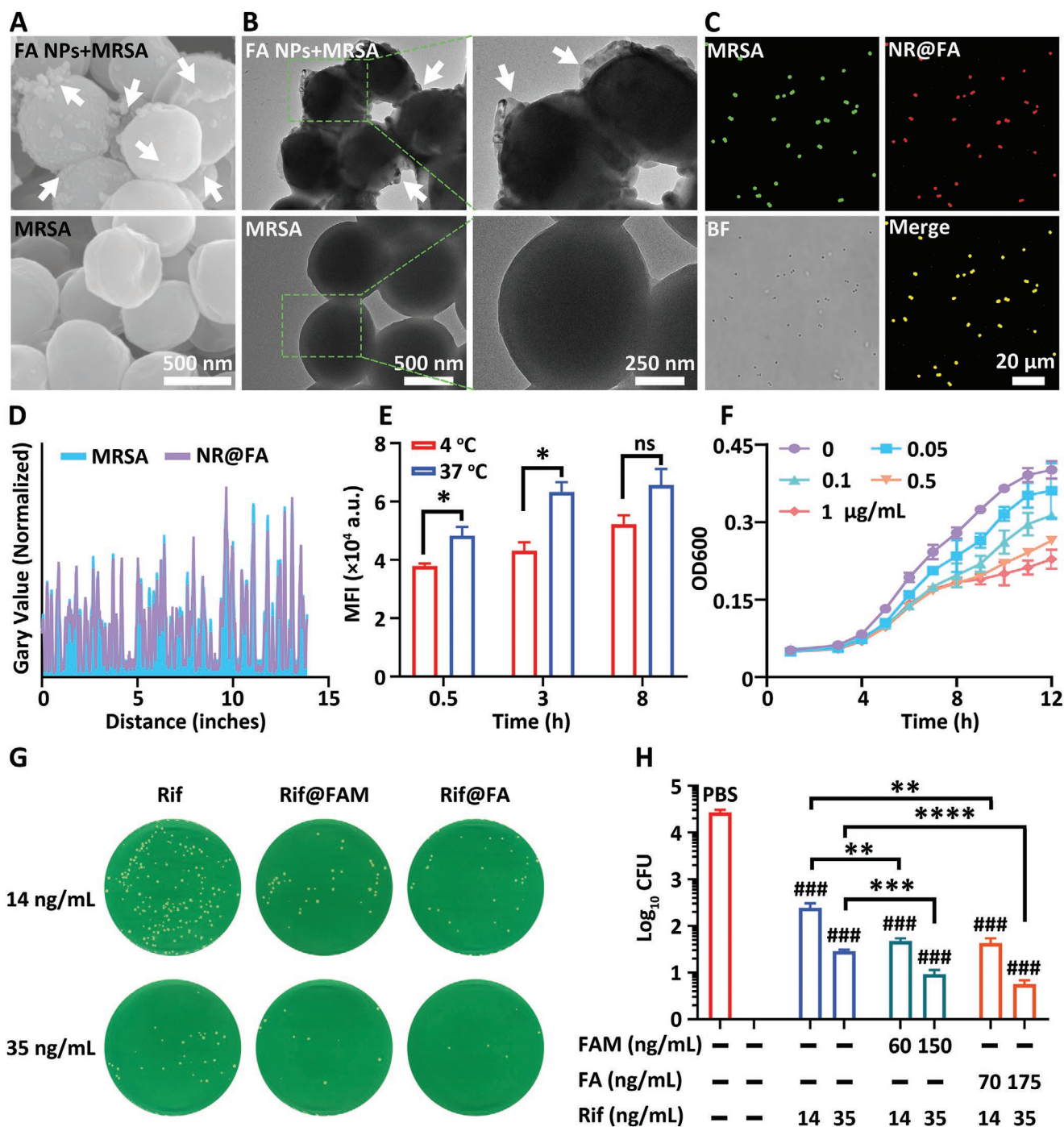
Figure 3. Bacterial targeting and extracellular antibacterial activity. A) SEM and B) TEM images of MRSA after incubation with/without FA NPs. The white arrows denote FA NPs attaching to the MRSA surface. C) Confocal images of FITC-labeled MRSA after incubation with NR@FA NPs for 3 h. D) Co-localization fluorescence intensity profiles between NR@FAM NPs and FITC-labeled MRSA, analyzed using Image J software. E) MFI of MRSA after incubation with FITC@FA NPs at 10 μg mL^{-1} for different times under different temperatures, determined by flow cytometry. F) Growth curves of MRSA against doses of FA NPs, $n = 3$. G) Photos of extracellular MRSA colonies after different treatments with 2 × minimum inhibitory concentration (2 × MIC, 14 ng mL^{-1}) and 5 × MIC (35 ng mL^{-1}). H) Colony-forming units (CFUs) of extracellular MRSA, $n = 3$. # means the contrasts between experimental groups and PBS. #/* $p < 0.05$, ##/** $p < 0.01$, ###/*** $p < 0.001$, **** $p < 0.0001$, and ns $p > 0.05$ respectively.

in-situ/ex-situ co-localization characteristics further confirmed the effective binding property of FAM DDS, demonstrating the FAM DDS possessed an intriguing feature of on-site antibiotic delivery.

Because of the ability of FAM NPs to efficiently target intracellular MRSA, we investigated their intracellular locations by monitoring the endocytic process of FTIC loaded FAM NPs (denoted as FITC@FAM NPs, **Figure 5**A). Their intracellular
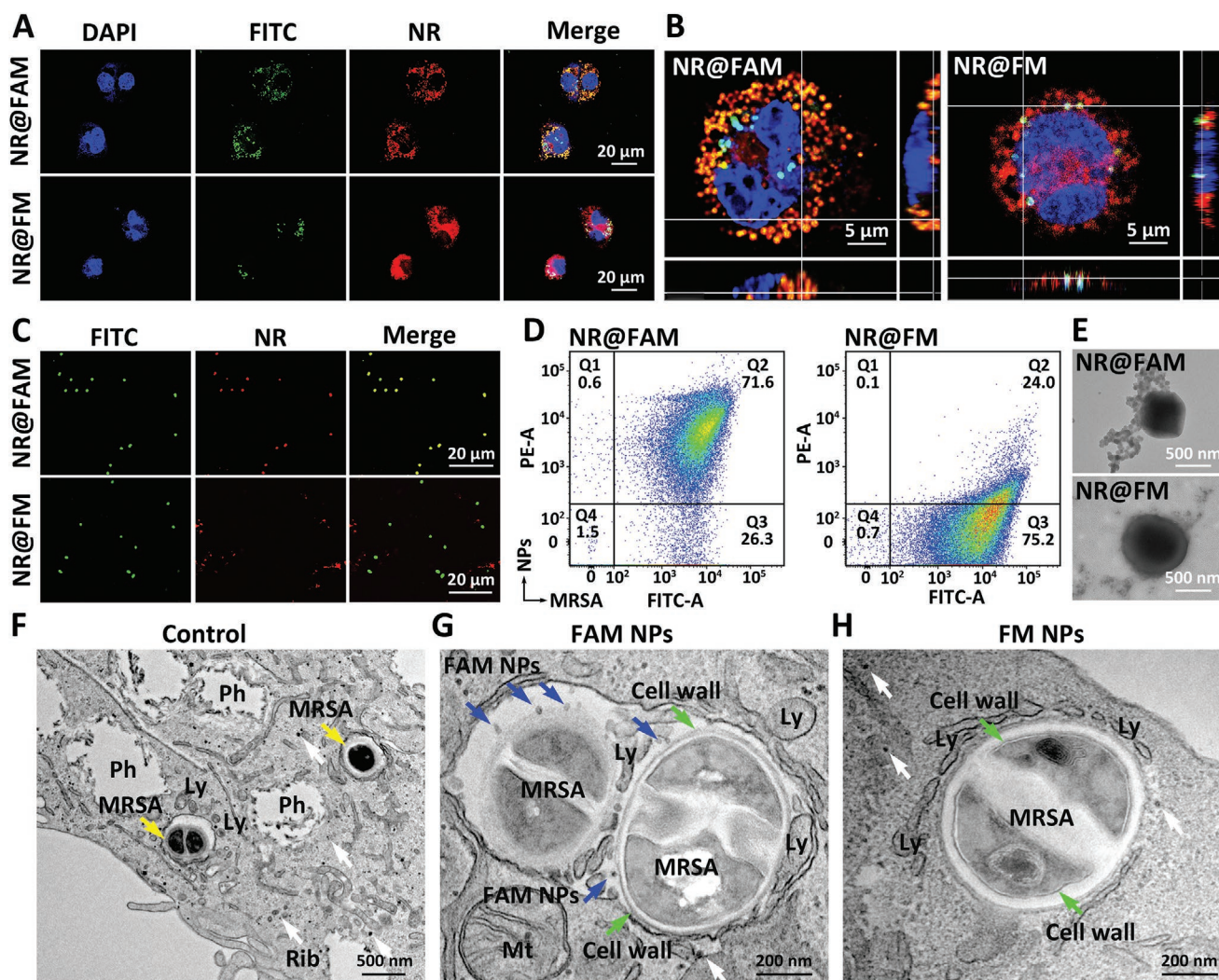
Figure 4. Intracellular bacteria targeting. A) Plane and B) z-stack confocal images of intracellular FITC-MRSA after incubation with NR@FAM and NR@FM NPs for 24 h. C) Confocal images, D) flow cytometry analysis, and E) TEM images of the separated intracellular MRSA after lysing the infected THP-1 macrophages by 0.1% Triton X-100. F–H) In situ TEM images of the MRSA in THP-1 macrophages after incubation with PBS (F), FAM NPs (G), and FM NPs (H) for 24 h. Ph: phagosome, Ly: lysosome, and Mt: mitochondria, Rib: ribosome (white arrows). MRSA (yellow arrows); cell wall (green arrows); FAM NPs (blue arrows).

locations were confirmed by co-localization with lysosomes, which were marked in red fluorescence by Lyso-Tracker Red dye. By fluorescence imaging, we found that the FITC@FAM NPs mainly accumulated in the cytoplasm in the first 0.5 and 1 h (Figure 5A). Quantitative analysis of the fluorescence signals revealed the overlap between FITC@FAM NPs and lysosomes was ≈40% (Figure 5B). With a longer incubation time, an increasing amount of FITC@FAM NPs was accumulated in lysosomes. Their co-localization reached up to ≈60% after 6 h incubation, suggesting that lysosomes were the main intracellular locations of FITC@FAM NPs. Extending the incubation time to 24 h, the amount of FITC@FAM NPs in lysosomes reduced to ≈38%, while more FITC@FAM NPs were found in the cytoplasm (Figure 5A), implying that FITC@FAM NPs could be further transported into the cytoplasm of macrophages.[29] This result was most likely attributed to the detachment of mannose from FAM NPs in the acidic environment of

lysosomes. The exposed amino groups in the resulting FA NPs boosted zeta potential (Figure S9, Supporting Information) and facilitated the transportation of the NPs from lysosomes to the cytoplasm,[30] which was crucial to exert cascade-targeting properties against intracellular infection.

Based on the results of the cellular internalization and extracellular antibacterial assays, we examined whether the novel cascade-targeting properties of Rif@FAM NPs are effective for killing intracellular bacteria (Figure 5C,D). THP-1 macrophages infected with MRSA were treated with Rif@FAM NPs and then analyzed by colony counting. Macrophage-targeted Rif@FM NPs, bacteria-targeted Rif@FA NPs, free Rif, and PBS were used as control groups. The concentration of Rif was set at 14 ng mL^{-1} (2 × MIC). Intracellular MRSA were suppressed in the presence of Rif at 12 h when compared with that in PBS group ($^{##}$, $p < 0.01$, Figure 5D). Additionally, the groups of Rif@FAM and Rif@FM NPs showed higher inhibition ability than
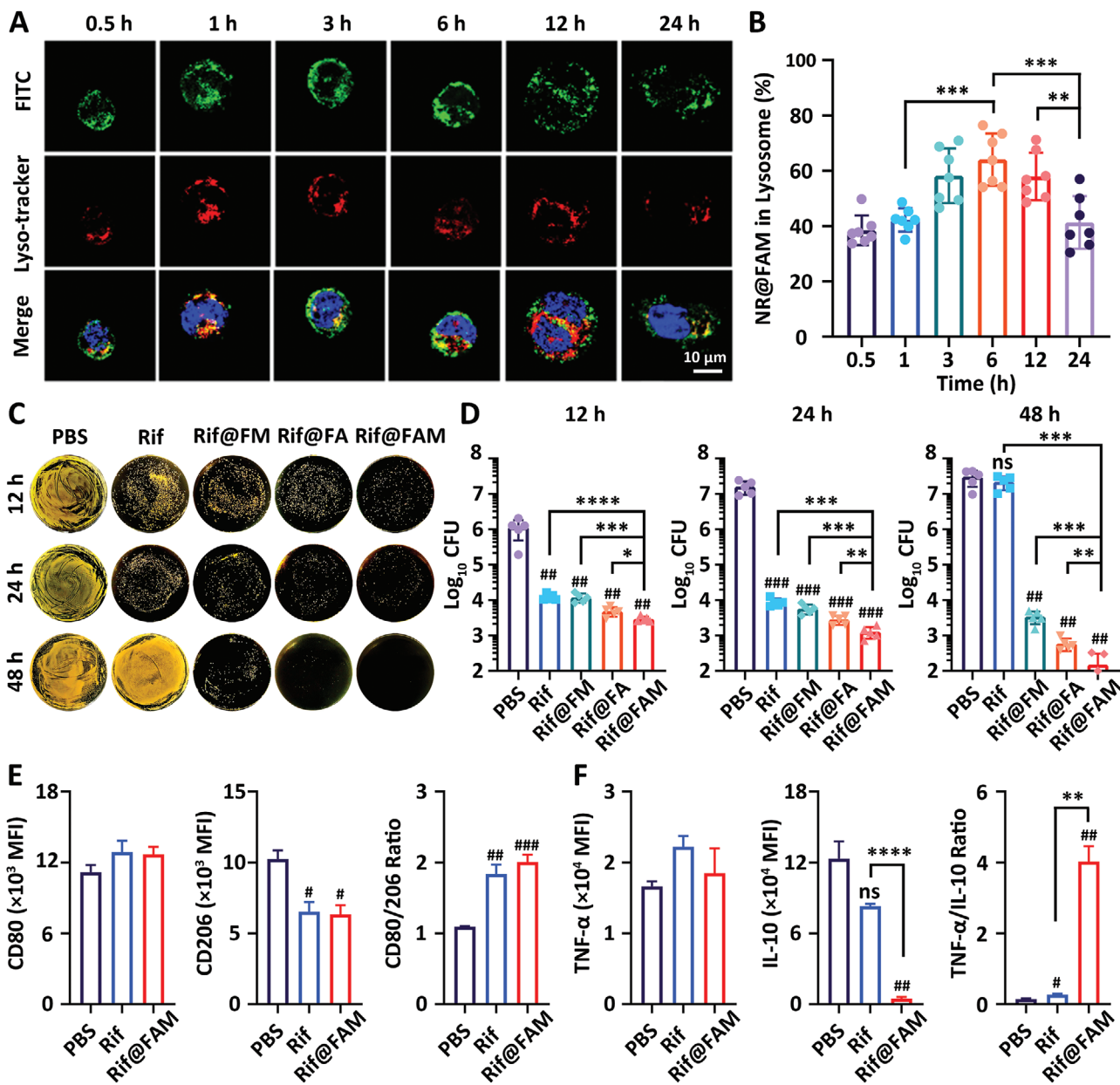
Figure 5. Intracellular antibacterial activity. A) Co-localization confocal images between FITC@FAM NPs and lysosomes after FITC@FAM NPs incubated with THP-1 macrophages for 0.5, 1, 3, 6, 12, and 24 h. B) Percentage of FITC@FAM NPs co-localized with lysosomes, $n = 7$. C) Photos and D) CFUs of intracellular MRSA with different treatments. The concentration of Rif was set at 14 ng mL^{-1} ($2 \times$ MIC), $n = 5$. E,F) The expression difference of CD80 and CD206 (E), and TNF-α and IL-10 (F) in MRSA-infected macrophages, determined by flow cytometry. $n = 3$. # means the contrasts between experimental groups and PBS. #/* $p < 0.05$, ##/** $p < 0.01$, ###/*** $p < 0.001$, **** $p < 0.0001$, and ns $p > 0.05$ respectively.

the free Rif at 24 h incubation, most likely due to their specific targeting of macrophages. Interestingly, Rif@FA exhibited a higher intracellular MRSA elimination performance than Rif@FM. This implied that penetrating across the cell membrane is critical, but routing antibiotics to the bacterial compartments may be more important for killing intracellular bacteria. Increasing the co-incubation time to 48 h, free Rif lost control of bacterial proliferation owing to its limited dosages and instability in the cells. In comparison, Rif@FAM NPs exhibited the highest intracellular bacterial inhibition efficacy (Figure 5D, ***, $p = 0.0006$ and **, $p = 0.007$ corresponded to the groups

of Rif@FM and Rif@FA NPs, respectively). This attributed that Rif@FAM NPs went through a novel cascade-targeting process and eliminated intracellular MRSA effectively via on-site Rif delivery.

Intracellular bacteria could resist the innate immune elimination by preventing pro-inflammatory macrophages polarization (M1, related to high antibacterial activity) and accelerating anti-inflammatory macrophages polarization (M2, produced inhibitory cytokines).[31] To determine whether the promising DDS modulates the polarization status of the infected macrophages, THP-1 macrophages were infected with MRSA and

further treated with Rif@FAM NPs, Rif, and PBS. Flow cytometry assay revealed that Rif@FAM NPs slightly upregulated the CD80 (an M1 marker) expression; whereas these significantly down-regulated the CD206 (an M2 marker, #, $p = 0.025$) expression in MRSA-infected THP-1 macrophages (Figure 5E and Figure S21, Supporting Information). The upregulated M1/M2 polarization reinforced the bacterial elimination ability of the infected macrophages. Additionally, the expression of representative immune cytokines TNF-α and IL-10 produced by M1 and M2 macrophages were further investigated. Appropriate but not overexpression of TNF-α is in favor of the production of antibacterial molecules;[32] while a high expression of IL-10 drives bacterial replication.[33] Rif@FAM NPs slightly increased TNF-α production and showed a notable decrease in IL-10 production compared with the PBS (##, $p = 0.007$) and free Rif group (****, $p = 0.0000002$, Figure 5F). Based on these results, we proposed that Rif@FAM NPs exhibited superior efficacy for eliminating intracellular bacteria via a synergistic effect, including a cascade-targeting drug delivery and upregulated the M1/M2 polarization of macrophages.

2.5. In Vivo Real-Time Tracking and Antibacterial Efficacy

The toxicity of FAM and Rif@FAM NPs in vivo was then evaluated. Female Balb/c mice (6–7 weeks) were treated with intravenous (i.v.) injection of the therapeutic dose (10 mg kg^{-1}) once every 2 days for 2 weeks. There was no death or loss of weight in all treatment groups (Figure S22, Supporting Information). After 2 weeks, the blood biochemistries of all the tested mice were analyzed. All indicators, including aspartate transaminase, alanine aminotransferase, alkaline phosphatase, gamma-glutamyl transferase, and blood urea nitrogen, serum albumin, total protein, creatinine, and total bilirubin, were similar to the control group, and showed no significant difference (Figure S22, Supporting Information). Besides, hematoxylin and eosin (H&E) staining of the major organs (heart, liver, spleen, lung, kidneys) exhibited normal histomorphology and no significant pathological abnormality (Figure S23, Supporting Information), suggesting that FAM and Rif@FAM NPs possessed good biocompatibility. Additionally, in vivo distribution of FAM NPs was assessed. Mice were i.v. injected with Cyanine 7.5-loaded FAM NPs (denoted as Cy7.5@FAM NPs), and monitored with an in vivo imaging system (IVIS). Cy7.5 signals were observed in the liver and spleen in 1 h and enhanced after 6 h treatment, whereas very weak signals were observed in other organs (Figure S24, Supporting Information).

To evaluate the in vivo targeting property of FAM NPs, a muscle infection model was used to determine the in vivo real-time distribution of FAM NPs.[34] As shown in **Figure 6**A, PBS (100 µL) and MRSA (5×10^7 CFU/mouse, 100 µL) were injected intramuscularly into the left thigh and right thigh (namely uninfected and infected sites), respectively. After 24 h treatment, Cy7.5@FAM NPs were administrated via i.v. injection and imaged by IVIS. Evident fluorescence signals were observed mainly distributing around the liver and the infected site at 1 h post-injection due to the EPR effect and cascade-targeting properties of FAM NPs (Figure 6B). Compared to the uninfected site, the fluorescence signal of the infected site showed a

gradual increase along with increasing time and finally reached the strongest at 24 h (Figure 6C). The major organs and tissues were collected for imaging after the 24 h treatment. The ex vivo biodistribution data indicated that Cy7.5@FAM NPs were mainly distributed in the liver, kidney, lung, and the infected site (Figure 6D,E). The MFI of the infected site was over tenfold more than that of the uninfected site (*, $p = 0.03$), suggesting FAM NPs could retain at the MRSA infected site by the specific targeting properties. All these results demonstrated that FAM-based DDS achieved on-site drug delivery in vivo.

The in vivo antibacterial efficacy of the DDS was evaluated in MRSA-induced peritonitis (Figure 6F), one of the representative intracellular infection models that is regarded as a "serious threat" by the U.S. CDC.[35] Different treatments were administered by peritoneal injection. After 24 h of the infection, total, extra-, and intracellular MRSA CFUs in the peritoneal fluid were determined (Figure 6G). For extracellular MRSA, Rif@FAM and Rif@FA NPs showed comparable elimination efficiency, and were better than free Rif and Rif@FM NPs due to their specific bacterial targeting property. Free Rif exhibited an appreciable extracellular bactericidal performance, but failed in suppressing intracellular MRSA owing to its limited intracellular concentration. Conversely, Rif@FAM NPs effectively killed the intracellular MRSA and showed the best therapeutic efficacy. The CFUs of surviving intracellular MRSA (Figure 6H) of Rif@FAM NPs (1.36 log$_{10}$CFU) were significantly lower than those of Rif@FA NPs (2.18 log$_{10}$CFU; **, $p = 0.004$) and Rif@FM NPs (3.24 log$_{10}$CFU; ***, $p = 0.0004$). Additionally, H&E analysis (Figure S25, Supporting Information) revealed that the lung and liver of the mouse in the PBS treated group displayed tissue injuries, such as the obvious heterogeneous widening of alveolar ducts in the lung, and the sinusoidal dilatation in the liver. In contrast, Rif@FAM NPs treatment visibly alleviated and even eliminated these tissue injuries, and there were no marked differences in the histological analysis results compared with the healthy group. Quantitative analysis of serum pro-inflammatory markers further confirmed that Rif@FAM NPs significantly attenuated tissue injury and inflammation (Figure S26, Supporting Information). This demonstrated that the cascade-targeting properties of Rif@FAM NPs had an excellent effect on the treatment of intracellular infection in vivo, which was consistent with the extracellular antibacterial assay results.

3. Conclusion

We have developed a novel DDS based on amphiphilic poly(*N*-acryloyl amino acid), FAM. This DDS possessed a specific cascade-targeting feature that targeted macrophages and intracellular MRSA in a sequential manner. Intracellular MRSA targeting and on-site Rif delivery endowed Rif@FAM NPs with appealing in vitro and in vivo performances of intracellular MRSA elimination, which distinctly outperformed the control groups of free Rif, Rif@FA, and Rif@FM NPs. The FAM-based DDS has superior advantages; i) high intracellular accumulation and long retention of antibiotics; ii) long term antibacterial activity because of the structural stability of the DDS against the harsh acidic environment; iii) precise on-site release of
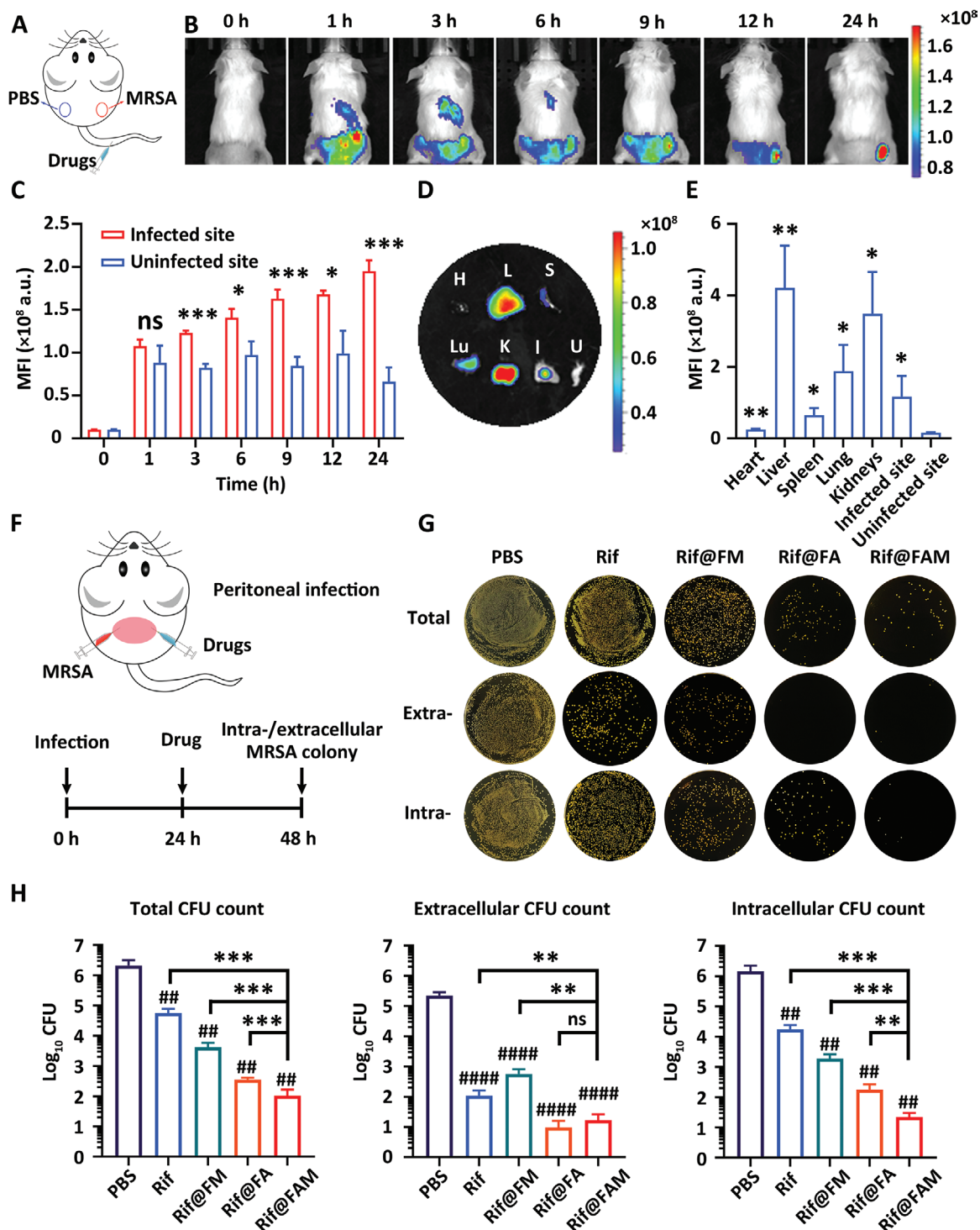
Figure 6. Targeted and antibacterial efficiency of the DDS in MRSA infected mice. A) Schematics of the infection model. The right thigh of the mice was administered with MRSA intramuscularly, denoted as the infected site. The left thigh was administered with PBS intramuscularly, denoted the uninfected site. Cy7.5@FAM NPs were administered by i.v. injection. B) The representative fluorescence images of the infected mice. C) MFI quantitative analysis of the infected and the uninfected sites. Statistical analysis was done for the infected site group to the uninfected site group, $n = 3$. D) Ex vivo fluorescence images of the major organs and tissues collected from the MRSA infected mice after 24 h i.v. injection. Heart, liver, spleen, lung, kidneys, the infected site, and the uninfected site are abbreviated as H, L, S, Lu, K, I, and U, respectively. E) MFI quantitative analysis of the organs or tissues in the ex vivo images. Statistical analysis was done for each organ against the uninfected site group, $n = 3$. F) Schematics of the MRSA peritonitis model. A single dose of Rif (10 mg kg^{-1}) was used for the antibacterial assays. G) Photos and H) CFUs in total, extra- and intracellular fractions were determined 24 h after the different treatments. $n = 5$. # means the contrasts between the experimental groups and PBS. #/* $p < 0.05$, ##/** $p < 0.01$, ###/*** $p < 0.001$, ####/**** $p < 0.0001$, and ns $p > 0.05$ respectively.

the antibiotics for eliminating intracellular bacteria regardless of their latent or dormant states; and iv) re-molding immune response of the infected-macrophages by the DDS reinforced antibacterial efficiency. Overall, this study offers proof-of-concept for efficiently eliminating intracellular bacteria via on-site antibiotic delivery using cascade-targeting DDSs.

Supporting Information

Supporting Information is available from the Wiley Online Library or from the author.

Conflict of Interest

The authors declare no conflict of interest.

Author Contributions

X.W. and G.L. conceived the project. X.W., G.L., and W.F. designed the experiments. W.F. and G.L. performed experimental work and analyzed the data with help of D.Z., H.L., Q.R., and T.F.M. In vivo assessments were performed with the help of X.K., F.L., and F.B. Antibacterial assays were performed with the help of R.W.. G.L., and W.F. drafted the manuscript. X.W., Y.Y., Q.R., and T.F.M. edited the manuscript. All the authors discussed the results and commented on the manuscript.

Data Availability Statement

Research data are not shared.

[1] a) J. Fu, Y. Li, Y. Zhang, Y. Liang, Y. Zheng, Z. Li, S. Zhu, C. Li, Z. Cui, S. Wu, *Adv. Mater.* **2021**, *33*, 2102926; b) P. Santucci, D. J. Greenwood, A. Fearns, K. Chen, H. Jiang, M. G. Gutierrez, *Nat. Commun.* **2021**, *12*, 3816; c) H.-K. Kwon, I. Lee, K. E. Yu, S. V. Cahill, K. D. Alder, Lee, S. C. M. Dussik, J. Back, J. Choi, L. Song, T. R. Kyriakides, F. Y. Lee, *Sci. Adv.* **2021**, *7*, eabf2665.

[2] a) X. Liu, F. Liu, S. Ding, J. Shen, K. Zhu, *Adv. Sci.* **2020**, *7*, 1900840; b) S. Trouillet-Assant, L. Lelièvre, P. Martins-Simões, L. Gonzaga, J. Tasse, F. Valour, J.-P. Rasigade, F. Vandenesch, R. L. Muniz Guedes, A. T. Ribeiro de Vasconcelos, J. Caillon, S. Lustig, T. Ferry, C. Jacqueline, G. Loss de Morais, F. Laurent, *Cell. Microbiol.* **2016**, *18*, 1405; c) C. Guarch-Pérez, M. Riool, S. A. Zaat, *Eur. Cells Mater.* **2021**, *41*, 334.

[3] a) Y. Wu, Y. Lin, Z. Cong, K. Chen, X. Xiao, X. Wu, L. Liu, Y. She, S. Liu, R. Zhou, G. Yin, X. Shao, Y. Dai, H. Lin, R. Liu, *Adv. Funct. Mater.* **2021**, 2107942; b) D. Huang, D. Li, T. Wang, H. Shen, P. Zhao, B. Liu, Y. You, Y. Ma, F. Yang, D. Wu, S. Wang, *Biomaterials* **2015**, *52*, 417.

[4] S. Maghrebi, P. Joyce, M. Jambhrunkar, N. Thomas, C. A. Prestidge, *ACS Appl. Mater. Interfaces* **2020**, *12*, 8030.

[5] F. Peyrusson, H. Varet, T. K. Nguyen, R. Legendre, O. Sismeiro, J.-Y. Coppée, C. Wolz, T. Tenson, F. Van Bambeke, *Nat. Commun.* **2020**, *11*, 2200.

[6] a) Y. M. Soe, S. Bedoui, T. P. Stinear, A. Hachani, *Cell. Microbiol.* **2021**, *23*, e13317; b) K. Ray, B. Marteyn, P. J. Sansonetti, C. M. Tang, *Nat. Rev. Microbiol.* **2009**, *7*, 333; c) R. S. Iannagan, G. Cosío, S. Grinstein, *Nat. Rev. Microbiol.* **2009**, *7*, 355.

[7] A. Moldovan, M. J. Fraunholz, *Cell. Microbiol.* **2019**, *21*, e12997.

[8] Y. Li, F. Liu, J. Zhang, X. Liu, P. Xiao, H. Bai, S. Chen, D. Wang, S. H. P. Sung, R. T. K. Kwok, J. Shen, K. Zhu, B. Z. Tang, *Adv. Sci.* **2021**, *8*, 2001750.

[9] a) M. Ye, Y. Zhao, Y. Wang, M. Zhao, N. Yodsanit, R. Xie, D. Andes, S. Gong, *Adv. Mater.* **2021**, *33*, 2006772; b) J. Trousil, O. Pavliš, P. Kubíčková, M. Škorič, V. Marešová, E. Pavlova, K. D. Knudsen, Y.-S. Dai, M. Zimmerman, V. Dartois, J.-Y. Fang, M. Hrubý, *J. Controlled Release* **2020**, *321*, 312; c) J. Pi, L. Shen, E. Yang, H. Shen, D. Huang, R. Wang, C. Hu, H. Jin, J. Cai, G. Zeng, Z. W. Chen, *Angew. Chem., Int. Ed.* **2020**, *59*, 3226.

[10] a) M.-H. Xiong, Y.-J. Li, Y. Bao, X.-Z. Yang, B. Hu, J. Wang, *Adv. Mater.* **2012**, *24*, 6175; b) J. Chen, F.-Y. Su, D. Das, S. Srinivasan, H.-N. Son, B. Lee, F. Radella, D. Whittington, T. Monroe-Jones, T. E. West, A. J. Convertine, S. J. Skerrett, P. S. Stayton, D. M. Ratner, *Biomaterials* **2019**, *195*, 38.

[11] a) R. Catania, F. Mastrotto, C. J. Moore, C. Bosquillon, F. H. Falcone, A. Huett, G. Mantovani, S. Stolnik, *Adv. Ther.* **2021**, *4*, 2100168; b) J. Pi, L. Shen, H. Shen, E. Yang, W. Wang, R. Wang, D. Huang, B.-S. Lee, C. Hu, C. Chen, H. Jin, J. Cai, G. Zeng, Z. W. Chen, *Mater. Sci. Eng., C* **2019**, *103*, 109777; c) Y. Li, N. Ariotti, B. Aghaei, E. Pandzic, S. Ganda, M. Willcox, M. Sanchez-Felix, M. Stenzel, *Angew. Chem., Int. Ed.* **2021**, *60*, 22652.

[12] a) S. M. Lehar, T. Pillow, M. Xu, L. Staben, K. K. Kajihara, R. Vandlen, L. DePalatis, H. Raab, W. L. Hazenbos, J. H. Morisaki, J. Kim, S. Park, M. Darwish, B.-C. Lee, H. Hernandez, K. M. Loyet, P. Lupardus, R. Fong, D. Yan, C. Chalouni, E. Luis, Y. Khalfin, E. Plise, J. Cheong, J. P. Lyssikatos, M. Strandh, K. Koefoed, P. S. Andersen, J. A. Flygare, M. W. Tan, et al., *Nature* **2015**, *527*, 323; b) S. Zhang, S. Zhou, H. Liu, M. Xing, B. Ding, B. Li, *ACS Appl. Mater. Interfaces* **2020**, *30*, 2002434.

[13] a) L. Huitema, T. Phillips, V. Alexeev, M. Tomic-Canic, I. Pastar, O. Igoucheva, *Exp. Dermatol.* **2021**, *30*, 1428; b) G. Mitchell, C. Chen, D. A. Portnoy, S. Gordon, *Microbiol. Spectrum* **2016**, *4*, 1.

[14] a) D. Kiran, B. K. Podell, M. Chambers, R. J. Basaraba, *Semin. Immunopathol.* **2016**, *38*, 167; b) S. Subramaniam, P. Joyce, N. Thomas, C. A. Prestidge, *Adv. Drug Delivery Rev.* **2021**, *177*,

113948; c) W. Yan, P. Banerjee, M. Xu, S. Mukhopadhyay, M. Ip, N. B. Carrigy, D. Lechuga-Ballesteros, K. K. W. To, S. S. Y. Leung, *Adv. Drug Delivery Rev.* **2021**, *176*, 113864.

[15] Y. Li, G. Yang, Y. Ren, L. Shi, R. Ma, H. C. van der Mei, H. J. Busscher, *Front. Chem.* **2020**, *7*, 861.

[16] G. Li, W. Feng, N. Corrigan, C. Boyer, X. Wang, J. Xu, *Polym. Chem.* **2018**, *9*, 2733.

[17] a) W. Feng, Z. Huang, X. Kang, D. Zhao, H. Li, G. Li, J. Xu, X. Wang, *Biomacromolecules* **2021**, *22*, 4871; b) W. Feng, G. Li, L. Tao, Y. Wei, X. Wang, *Colloids Surf., B* **2021**, *202*, 111687.

[18] J. R. Casey, S. Grinstein, J. Orlowski, *Nat. Rev. Mol. Cell Biol.* **2010**, *11*, 50.

[19] P. Yuan, Z. Ruan, T. Li, Y. Tian, Q. Cheng, L. Yan, *J. Mater. Chem. B* **2019**, *7*, 6770.

[20] K. Bauri, M. Nandi, P. De, *Polym. Chem.* **2018**, *9*, 1257.

[21] X. Yang, B. Xie, H. Peng, G. Shi, B. Sreenivas, J. Guo, C. Wang, Y. He, *J. Controlled Release* **2021**, *329*, 454.

[22] M. G. Elnaggar, K. Jiang, H. E. Eldesouky, Y. Pei, J. Park, S. A. Yuk, F. Meng, A. M. Dieterly, H. T. Mohammad, Y. A. Hegazy, H. M. Tawfeek, A. A. Abdel-Rahman, A. E. Aboutaleb, M. N. Seleem, Y. Yeo, *Biomaterials* **2020**, *262*, 120344.

[23] a) F. Hu, G. Qi, Kenry, D. Mao , S. Zhou, M. Wu, W. Wu, B. Liu, *Angew. Chem., Int. Ed.* **2020**, *59*, 9288; b) Y.-P. Hsu, E. Hall, G. Booher, B. Murphy, A. D. Radkov, J. Yablonowski, C. Mulcahey, L. Alvarez, F. Cava, Y. V. Brun, E. Kuru, M. S. VanNieuwenhze, *Nat. Chem.* **2019**, *11*, 335; c) P. Shieh, M. S. Siegrist, A. J. Cullen, C. R. Bertozzi, *Proc. Natl. Acad. Sci. USA* **2014**, *111*, 5456.

[24] C. A. Marangon, V. C. A. Martins, M. H. Ling, C. C. Melo, A. M. G. Plepis, R. L. Meyer, M. Nitschke, *ACS Appl. Mater. Interfaces* **2020**, *12*, 5488.

[25] a) X. Yang, Y. Dang, M. J. Lou, H. Shao, X. Jiang, *Theranostics* **2018**, *8*, 1449; b) T. J. Lupoli, H. Tsukamoto, E. H. Doud, T.-S. A. Wang, S. Walker, D. Kahne, *J. Am. Chem. Soc.* **2011**, *133*, 10748.

[26] E. Kuru, S. Tekkam, E. Hall, Y. V. Brun, M. S. Van Nieuwenhze, *Nat. Protoc.* **2015**, *10*, 33.

[27] Y. Zhu, J. Zhang, J. Song, J. Yang, Z. Du, W. Zhao, H. Guo, C. Wen, Q. Li, X. Sui, L. Zhang, *Adv. Funct. Mater.* **2020**, *30*, 1905493.

[28] L. I. FitzGerald, L. Aurelio, M. Chen, D. Yuen, J. J. Rennick, B. Graham, A. P. R. Johnston, *Nat. Commun.* **2020**, *11*, 4482.

[29] Q. Zhou, J. Xiang, L. Hao, X. Xu, Z. Zhou, J. Tang, Y. Ping, Y. Shen, *Nano Today* **2021**, *39*, 101221.

[30] S. Roy, D. Zhu, W. J. Parak, N. Feliu, *ACS Nano* **2020**, *14*, 8012.

[31] a) M. Benoit, B. Desnues, J.-L. Mege, *J. Immunol.* **2008**, *181*, 3733; b) J. Lee, H. Byun, S. K. Madhurakkat Perikamana, S. Lee, H. Shin, *Adv. Healthcare Mater.* **2019**, *8*, 1800861.

[32] A. M. Cooper, S. A. Khader, *Immunol. Rev.* **2008**, *226*, 191.

[33] S. Gordon, *Nat. Rev. Immunol.* **2003**, *3*, 23.

[34] M. Ye, Y. Zhao, Y. Wang, N. Yodsanit, R. Xie, S. Gong, *Adv. Funct. Mater.* **2020**, *30*, 2002655

[35] a) Y. Li, Y. Liu, Y. Ren, L. Su, A. Li, Y. An, V. Rotello, Z. Zhang, Y. Wang, Y. Liu, S. Liu, J. Liu, J. D. Laman, L. Shi, H. C. van der Mei, H. J. Busscher, *Adv. Funct. Mater.* **2020**, *30*, 2004942; b) C. D. C. Prevention, *Antibiotic Resistance Threats in the United States, 2019*, US Department of Health and Human Services, Atlanta, GA, USA **2019**.